Eur. Phys. J. E **32**, 339–348 (2010)
DOI 10.1140/epje/i2010-10629-8

THE EUROPEAN PHYSICAL JOURNAL E

Regular Article

Simulation of flow of mixtures through anisotropic porous media using a lattice Boltzmann model

M. Mendoza[a], F.K. Wittel, and H.J. Herrmann

ETH Zurich, Institute for Building Materials, Computational Physics for Engineering Materials, Schafmattstrasse 6, HIF, CH-8093 Zurich, Switzerland

Received 17 November 2009 and Received in final form 11 May 2010
Published online: 4 August 2010 –

Abstract. We propose a description for transient penetration simulations of miscible and immiscible fluid mixtures into anisotropic porous media, using the lattice Boltzmann (LB) method. Our model incorporates hydrodynamic flow, advection-diffusion, surface tension, and the possibility for global and local viscosity variations to consider various types of hardening fluids. The miscible mixture consists of two fluids, one governed by the hydrodynamic equations and one by advection-diffusion equations. We validate our model on standard problems like Poiseuille flow, the collision of a drop with an impermeable, solid interface and the deformation of the fluid due to surface tension forces. To demonstrate the applicability to complex geometries, we simulate the invasion process of mixtures into wood spruce samples.

1 Introduction

Fluid invasion and flow in porous media are ubiquitous phenomena in nature and technology. In principle, studies on porous media can be classified by three length scales: the pore scale, the representative volume element (RVE) scale, and the domain scale [1]. Studies on the pore scale directly model the pore space geometry and the fluid hydrodynamics [2]. The intermediate sized RVE is the minimum volume required to characterize the flow through the medium, *e.g.* with complex pore space geometry. Typical examples are the Darcy, the Brinkman-extended Darcy, and the Forchheimer-extended Darcy models [1]. The flow in porous media can also be modeled via generalized Navier-Stokes equations [3–5], including all necessary terms in one momentum conservation equation. Unfortunately in the majority of cases, the analytical solution becomes very difficult and is even more complicated for anisotropic, structured porous media like wood. Therefore, one depends on numerical methods in this field. The fluid itself can be quite complicated as well. It can be a miscible or immiscible mixture of different species, its viscosity can change locally due to internal chemical reactions like hardening and can depend on shear velocities in the case of non-Newtonian fluids. Examples are adhesive penetration at wood junctures or the impregnation or sealing of concrete for protective reasons. A practical model approach for these phenomena is hydrodynamic dispersion [6] that treats one fluid, *e.g.* a solvent, by the hydrodynamic theory and the others, *e.g.* solutes, by advection-diffusion equations. For complicated anisotropic porous media and fluids, coupling the advection-diffusion with the generalized Navier-Stokes equations makes analytical solutions quite difficult. The motivation for the present work is adhesive penetration in wood.

Wood constructions depend on good adhesive bondings, that are the result of a gluing process, where hardening liquids are pressed into a porous, anisotropic micro structure. Depending on the penetration and adhesive hardening characteristics, preferrable interface morphologies can be obtained [7]. The penetration is dominated by the strong anisotropy of the permeability tensor and the viscosity evolution of the adhesive. Due to the difficulty of the problem, penetration simulations with classical continuum mechanics are hardly feasible.

Over the last two decades, lattice Boltzmann (LB) methods developed to be an alternative to the simulation of partial differential equations (PDEs). Originally, LB methods were developed as discrete realizations of kinetic models for fluids [8,9]. Extensions allow for the simulation of advection-diffusion [10], waves [11,12], magnetohydrodynamics [13–15], quantum mechanics [16], and multiphase flows [17–22]. Tölke *et al.* [23] construct a three-dimensional lattice Boltzmann model for immiscible binary fluids with variable viscosity and density ratio based on the work by Gunstensen [22]. The authors consider two immiscible fluids that evolve inside a pore scale system by the Navier-Stokes equations with interaction terms. LB models for incompressible flows through porous media on the RVE scale were first addressed by Guo *et al.* [24], who proposed a 2D model including a nonlinear Forchheimer term, that can be used for isotropic, heterogeneous porous media.

[a] e-mail: mmendoza@ethz.ch

We introduce a 3D LB model that recovers the generalized Navier-Stokes equations in anisotropic porous media, extended by the advection-diffusion equation for the solute concentration in fluid mixtures. Consequently, viscosity changes appear that can be superimposed by local hardening. Additionally, we incorporate the free surface technique [25] to allow for immiscible fluids. In this paper, sect. 2 first describes some LB fundamentals and the numerical model details for fluid and diffusive particles. Section 3 shows a brief description of the free surface technique, while sect. 4 addresses the implementation of the algorithm and sect. 5 demonstrates the validity of our model and its application to diverse physical systems.

2 Lattice-Boltzmann model for 3D anisotropic porous media

The generalized Navier-Stokes equations [1] for incompressible fluids and low Reynolds numbers are the starting point, expressing mass conservation

$$\nabla \cdot \mathbf{V} = 0, \tag{1}$$

and momentum conservation

$$\frac{\partial \mathbf{V}}{\partial t} + (\mathbf{V}\cdot\nabla)\left(\frac{\mathbf{V}}{\epsilon}\right) = -\frac{1}{\rho}\nabla(\epsilon P) + \nu_e \nabla^2 \mathbf{V} + \epsilon \mathbf{G} - \epsilon\nu \mathsf{K}^{-1}\cdot\mathbf{V} - \frac{\epsilon}{\rho}\nabla\cdot\mathsf{S}. \tag{2}$$

Here ρ denotes fluid density, ν the viscosity, $\mathbf{V}$ the volume-averaged velocity and P the pressure. ϵ stands for the porosity of the medium, K for the (anisotropic) permeability tensor, and $\mathbf{G}$ represents an external force field. Note that the effective viscosity ν_e is not expected to be the same as the viscosity of the fluid due to tortuosity effects and dispersion of viscous advection-diffusion flux [1]. The hydrostatic pressure P is related to the density via $P = \rho c_s^2/\epsilon$, with the speed of sound of the fluid c_s. In order to control the surface tension at the liquid-gas interface, we add the last term in eq. (2), based on the diffusive interface method proposed by Korteweg [26]. Originally, this method was not applied to a liquid-gas interface inside a porous medium, however in our model it minimizes the surface area of the interface quite well. The surface tension tensor S can be expressed in terms of the density gradient $\mathbf{F} = \nabla\rho$ as [27,28]

$$\mathsf{S} \approx B\left(|\mathbf{F}|^2 \mathsf{I} - \mathbf{F}\otimes\mathbf{F}\right), \tag{3}$$

where B denotes a gradient energy coefficient [28], which is usually taken as constant, I is the identity matrix and $\otimes$ represents the outer product. To consider wetting properties in terms of the contact angle θ, we need to calculate the surface tension σ_{lg} for a liquid-gas interface. σ_{lg} is related to the constant B and the density gradient by

$$\sigma_{lg} = B\int |\mathbf{F}|^2 \mathrm{d}l \sim B\frac{|\Delta\rho|^2}{\Delta l}, \tag{4}$$

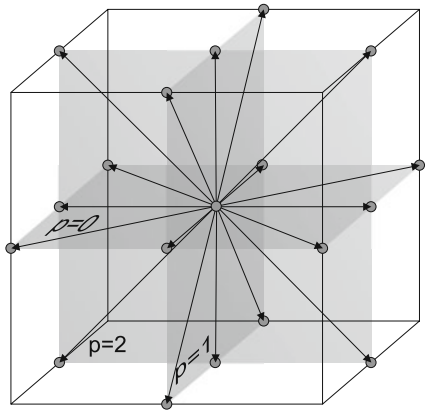

Fig. 1. Cubic lattice D3Q19 discretization. The arrows represent the velocity vectors $\mathbf{v}_i^p$, where p indicates the plane of location. Note that by including the rest vector located in the center of the cell, totally 19 directions are defined.

where l is a coordinate normal to the interface and Δl denotes the diffusive interface thickness. To calculate wettability properties of a solid substrate by the liquid, we have to consider the solid-liquid interface energy via the surface tension σ_{sl}. This interaction should be included in the surface tension tensor S. According to the literature, the contact angle θ is defined by

$$\cos(\theta) = \frac{\sigma_{sg} - \sigma_{sl}}{\sigma_{lg}}, \tag{5}$$

with the surface tension σ_{sg} of the solid-gas interface. However, for simplicity, we include the wettability only by considering the surface tension σ_{lg} and the difference $\sigma_s = \sigma_{sl} - \sigma_{sg}$, and calculate the contact angle

$$\cos(\theta) = -\frac{\sigma_s}{\sigma_{lg}}. \tag{6}$$

It is important to note that if we know the contact angle for a given system and its surface tension σ_{lg}, the quantity σ_s is determined by using eq. (6).

In the following we demonstrate how Navier-Stokes equations are reproduced by LB methods, and how extensions like external forces, Darcy flow, and surface tension can be added to the framework. Advection-diffusion, however, is treated in a separate section.

2.1 Model description for the generalized Navier-Stokes equations

The basic idea of LB models is that Navier-Stokes equations are not solved directly on a grid of cells, but via a strongly simplified particle micro dynamics with discrete Boltzmann equations and collision rules such as the Bhatnagar-Gross-Krook (BGK) [29]. The two ingredients particle streaming and collision are calculated along a certain number of fixed orientations in each cubic cell with lattice constant $\delta x = \delta t$ (19 in our case as illustrated in fig. 1). The velocity vectors are denoted by $\mathbf{v}_i^p$, where

$i = 1, \ldots, 6$, indicates their orientation and $p = 0, 1, 2$ their reference plane (see fig. 1). Each velocity vector $\mathbf{v}_i^p$ comes along with one assigned distribution function f_i^p. The density ρ in a cell is the sum over its distribution functions

$$\rho = \sum_{i=1}^{6} \sum_{p=0}^{2} f_i^p. \tag{7}$$

We obtain continuum properties for $\mathbf{V}$ and $\mathbf{F}$ via

$$\rho \mathbf{V} = \sum_{i=1}^{6} \sum_{p=0}^{2} f_i^p \mathbf{v}_i^p, \qquad \mathbf{F} = \sum_{i=1}^{6} \sum_{p=0}^{2} \rho(\mathbf{x} + \mathbf{v}_i^p) \mathbf{v}_i^p. \tag{8}$$

In order to include the influence of the porous media, of external forces, and of surface tension on the momentum equation (eq. (2)), we need to include additional force terms in the LB model. Following the work of Guo *et al.* [30], we add two force terms, T_0 for the zero velocity, and T_i^p for the remaining 18 non-zero velocities as follows:

$$\begin{aligned} f_i^p(\mathbf{x} + \mathbf{v}_i^p, t+1) - f_i^p(\mathbf{x}, t) &= \Omega_i^p(\mathbf{x}, t) + T_i^p, \\ f_0(\mathbf{x}, t+1) - f_0(\mathbf{x}, t) &= \Omega_0(\mathbf{x}, t) + T_0. \end{aligned} \tag{9}$$

The second ingredient of LB are the BGK collision terms Ω_i^p and Ω_0 [29], namely,

$$\Omega_i^p = -\frac{1}{\tau}(f_i^p(\mathbf{x}, t) - f_i^{p,\mathrm{eq}}(\mathbf{x}, t)),$$

and

$$\Omega_0 = -\frac{1}{\tau}(f_0(\mathbf{x}, t) - f_0^{\mathrm{eq}}(\mathbf{x}, t)), \tag{10}$$

with the characteristic relaxation time τ, that is fixed by the effective viscosity $\nu_e = \frac{1}{3}(\tau - \frac{1}{2})$, in lattice units. The subscript $^{\mathrm{eq}}$ denotes the equilibrium states for the distribution functions, which we must find such that the model reproduces correctly the hydrodynamic equations. The force terms T_i^p and T_0 are given by [30]

$$\begin{aligned} T_i^p &= \left(1 - \frac{1}{2\tau}\right)\left(3(\mathbf{v}_i^p \cdot \mathbf{F}^{ext}) \right. \\ &\quad \left. + \frac{9}{\epsilon}(\mathbf{v}_i^p \cdot \mathbf{V}')(\mathbf{v}_i^p \cdot \mathbf{F}^{ext}) - \frac{3}{\epsilon}(\mathbf{V}' \cdot \mathbf{F}^{ext})\right), \\ T_0 &= \left(1 - \frac{1}{2\tau}\right)\left(-\frac{3}{\epsilon}\mathbf{V}' \cdot \mathbf{F}^{ext}\right), \end{aligned} \tag{11}$$

with the external force $\mathbf{F}^{ext}$ which is in our case

$$\mathbf{F}^{ext} = -\epsilon\nu \mathsf{K}^{-1} \cdot \mathbf{V}' + \epsilon \mathbf{G}. \tag{12}$$

Due to the external forces, the velocity $\mathbf{V}$ needs to be corrected to obtain $\mathbf{V}'$ by

$$\mathbf{V}' = \mathbf{V} + \frac{1}{2}\mathbf{F}^{ext}. \tag{13}$$

Unfortunately, $\mathbf{F}^{ext}$ depends on $\mathbf{V}'$. By inserting eq. (12) into eq. (13), we obtain

$$\mathbf{V}' = \Lambda^{-1} \cdot \left(\mathbf{V} + \frac{1}{2}\mathbf{G}\right), \tag{14}$$

where we define $\Lambda = \mathsf{I} + \frac{\epsilon\nu}{2}\mathsf{K}^{-1}$ with the identity matrix I.

The final equilibrium functions for our system are:

$$\begin{aligned} f_i^{p,\mathrm{eq}}(\mathbf{x}, t) = w_i \rho \Bigg[& 1 + 3(\mathbf{v}_i^p \cdot \mathbf{V}') + \frac{9}{2\epsilon}(\mathbf{v}_i^p \cdot \mathbf{V}')^2 \\ & - \frac{3}{2\epsilon}\mathbf{V}'^2 + \frac{A\epsilon\tau}{\rho}\left(\frac{(\mathbf{v}_i^p \cdot \mathbf{F})^2}{|\mathbf{F}|} - |\mathbf{F}|\right)\Bigg], \end{aligned} \tag{15}$$

$$f_0^{\mathrm{eq}}(\mathbf{x}, t) = w_0 \rho \left[1 - \frac{3}{2\epsilon}\mathbf{V}'^2\right] + A\epsilon\tau w_0 |\mathbf{F}|, \tag{16}$$

with the known weights $w_0 = 1/3$, $w_{1,2,3,4} = 1/36$, and $w_{5,6} = 1/18$ for the D3Q19 cells [31]. To consider surface tension in the momentum conservation equation (eq. (2)), we have to express the tensor S by

$$\mathsf{S} = \frac{2A\tau}{9|\mathbf{F}|} \cdot \begin{pmatrix} -F_y^2 - F_z^2 & F_x F_y & F_x F_z \\ F_x F_y & -F_x^2 - F_z^2 & F_y F_z \\ F_z F_x & F_z F_y & -F_x^2 - F_y^2 \end{pmatrix}, \tag{17}$$

with the density gradient $\mathbf{F} = \nabla\rho$, a parameter A that fixes the strength of the surface tension, and the characteristic relaxation time τ. To describe the correct wetting properties of both, liquid-gas and solid-gas interfaces, we have to set the values for A, for the liquid-gas interface $A = A_g$ using the relation $A_g = \frac{9B|\mathbf{F}|}{2\tau}$ and eq. (4), while for the liquid-solid interface $A = A_s$ with

$$A_s = -A_g \cos(\theta). \tag{18}$$

Therefore, we must distinguish between cells with a liquid-solid interface, and the ones with a liquid-gas interface.

Via Chapman-Enskog expansion it can be shown that the surface tension tensor S is reproduced in the continuum limit (not shown). Also it can be shown analytically [32] that this LB-BGK model recovers the generalized Navier-Stokes equations eqs. (1), (2) in the isothermal and incompressible limit including surface tension.

2.2 Lattice Boltzmann model for solute advection-diffusion

To consider advection-diffusion in an LB framework for solute concentration in fluid mixtures, we can either define an additional set of velocity vectors and include their diffusive terms directly into the equilibrium function (eq. (15)), or define additional equilibrium distribution functions for the advection-diffusion but work on the same velocity vectors as proposed by Hiorth *et al.* [33] on a D2Q9 cell configuration. In this work, the second approach was chosen, to simplify a later extension to various fluid species and we recover the advection-diffusion equation in porous media based on ref. [33], but extend it to heterogeneous porous media. Starting from the advection-diffusion equation

$$\frac{\partial C}{\partial t} + \nabla \cdot (C\mathbf{U}) = \nabla \cdot [D \nabla C], \tag{19}$$

with the concentration C, the diffusivity D, and the velocity of the mixture $\mathbf{U}$, Hiorth *et al.* [33] define a distribution

function h_i for each velocity vector. The concentration is calculated via $C = \sum_{i=1}^{9} h_i$ and the equilibrium equations are defined by

$$h_i^{\mathrm{eq}}(\mathbf{x},t) = w_i C[1 + 3(\mathbf{v}_i^p \cdot \mathbf{U})], \quad h_0^{\mathrm{eq}}(\mathbf{x},t) = w_0 C, \quad (20)$$

with the weights $w_0 = 4/9$, $w_{1,2,3,4} = 1/9$, and $w_{5,6,7,8} = 1/36$ [33]. To make the extension to 3D and to include the porous medium, we propose modified equilibrium distribution functions on a D3Q19 cell configuration (see fig. 1)

$$h_i^{p,\mathrm{eq}}(\mathbf{x},t) = w_i \epsilon C[1 + 3(\mathbf{v}_i^p \cdot \mathbf{V}^*)], \quad h_0^{\mathrm{eq}}(\mathbf{x},t) = w_0 \epsilon C, \quad (21)$$

where $\mathbf{V}^* = \mathbf{V}' + D\frac{\nabla\epsilon}{\epsilon}$. With the correct weights $w_{0,i}$ for the D3Q19 cell, we evolve eq. (21) according to the Boltzmann equation with the BGK collision term $\Omega_{Di}^p(\mathbf{x},t)$ [29]:

$$\begin{aligned} &h_i^p(\mathbf{x}+\mathbf{v}_i, t+1) - h_i^p(\mathbf{x},t) = \Omega_{Di}^p(\mathbf{x},t), \\ &\Omega_{Di}(\mathbf{x},t) = -\frac{1}{\tau_D}(h_i^p(\mathbf{x},t) - h_i^{p,\mathrm{eq}}(\mathbf{x},t)). \end{aligned} \quad (22)$$

Now τ_D defines the relaxation time for the advection-diffusion model with the diffusivity, $D = \frac{1}{3}(\tau_D - \frac{1}{2})$. We can prove via a Chapmann-Enskog expansion that the model reproduces

$$\frac{\partial(\epsilon C)}{\partial t} + \nabla \cdot (\epsilon C \mathbf{V}') = \nabla \cdot [\epsilon D \nabla C] \quad (23)$$

in the continuum limit.

The full model can now reproduce the generalized Navier-Stokes equations in the continuum limit for anisotropic porous media, including surface tension and the diffusion-advection of the solute. To complete the description of the model, we will briefly summarize the free surface technique [25] used to describe the movement of the fluid with a fluid-gas interface.

3 The free surface technique

If a fluid penetrates an unsaturated porous medium, free surfaces form. That needs to be included in our LB scheme via the free surface technique [25]. Although it was not intended to model the liquid-gas interface inside porous media, we can extend the free surface technique to be applicable to our model. This is possible since the aim of the technique is to ensure the pressure balance across the interface independent of the underlying pore space. If a cell is only filled by gas with a negligible density, eqs. (15) and (16) lead to vanishing equilibrium functions and the simulation becomes unstable. This problem can be solved by classifying fluid cells into three types: the liquid cells, totally filled by liquid fluid, the empty cells entirely filled by gas, and the interface cells that contain both, liquid and gas. The purely liquid-filled cells were discussed in the previous section, while gas-filled cells can be excluded from the further calculation due to the high-density ratio between fluid and gas. However, the interface cells need further attention.

Interface cells consist partially of liquid and of gas, determined by the fluid fraction $\lambda(\mathbf{x},t) = m(\mathbf{x},t)/\rho(\mathbf{x},t)$ with the mass m of liquid in the cell located in $\mathbf{x}$ at time t. Using a normalized cell volume, the mass for the fluid cell is equal to the density of the liquid, and for gas cells equal to zero. Analogous to eq. (7), we obtain the macroscopic mass $m(\mathbf{x},t)$ by summing the mass functions m_i^p over all directions

$$m(\mathbf{x},t) = \sum_{i=1}^{6}\sum_{p=0}^{2} m_i^p. \quad (24)$$

The mass functions m_i^p evolve according to

$$m_i^p(\mathbf{x}, t+1) = m_i^p(\mathbf{x},t) + \sum_{i=1}^{6}\sum_{p=0}^{2} \Delta m_i^p(\mathbf{x}, t+1), \quad (25)$$

with

$$\begin{aligned} \Delta m_i^p(\mathbf{x}, t+1) = {} & f_j^p(\mathbf{x}+\mathbf{v}_i^p, t)\frac{\lambda(\mathbf{x}+\mathbf{v}_i^p,t) + \lambda(\mathbf{x},t)}{2} \\ & - f_i^p(\mathbf{x},t)\frac{\lambda(\mathbf{x}+\mathbf{v}_i^p,t) + \lambda(\mathbf{x},t)}{2}, \end{aligned} \quad (26)$$

where the index j stands for the vector with opposite direction to the vector with index i. The interface cells also have associated distribution functions that evolve via the discrete Boltzmann eq. (9) identical to those in the fluid cells. These distribution functions are used to calculate the density and the updated fluid fraction λ.

Nevertheless, we still obtain zero distribution functions in the interface cells from eq. (9), due to empty neighboring cells. To avoid this problem, we calculate the evolution of distribution functions of interface cells originating from empty neighboring cells with the modified function

$$f_j^p(\mathbf{x}, t+1) = f_i^{p,\mathrm{eq}}(\mathbf{x},t) + f_j^{p,\mathrm{eq}}(\mathbf{x},t) - f_i^p(\mathbf{x},t). \quad (27)$$

During the system evolution, the interface moves, leading to changes in the fluid fraction λ. If λ becomes unity, the cell changes to a liquid cell, while $\lambda \to 0$ leads to gas or empty cells. To complete the picture all cells neighboring new liquid cells are set to interface cells. Note that pressure balance on the gas-liquid interface is a consequence of the surface tension. However, when the liquid-gas density ratio is larger than say 100, surface tension techniques fail to balance the pressure difference in lattice Boltzmann methods. As a consequence, to minimize the surface area and equilibrate the pressure difference on the liquid-gas interface, including the wettability properties of solid materials, we use a combination of the free surface and surface tension techniques.

To summarize, by classifying cell types and corresponding distribution functions, according to fluid type, we can capture the evolution of free surfaces. A more detailed description can be found in ref. [25]. Finally this technique extends our model to simulations of fluid penetration with gas/liquid interface. Before validation examples are shown, we outline the implementation of the algorithm.

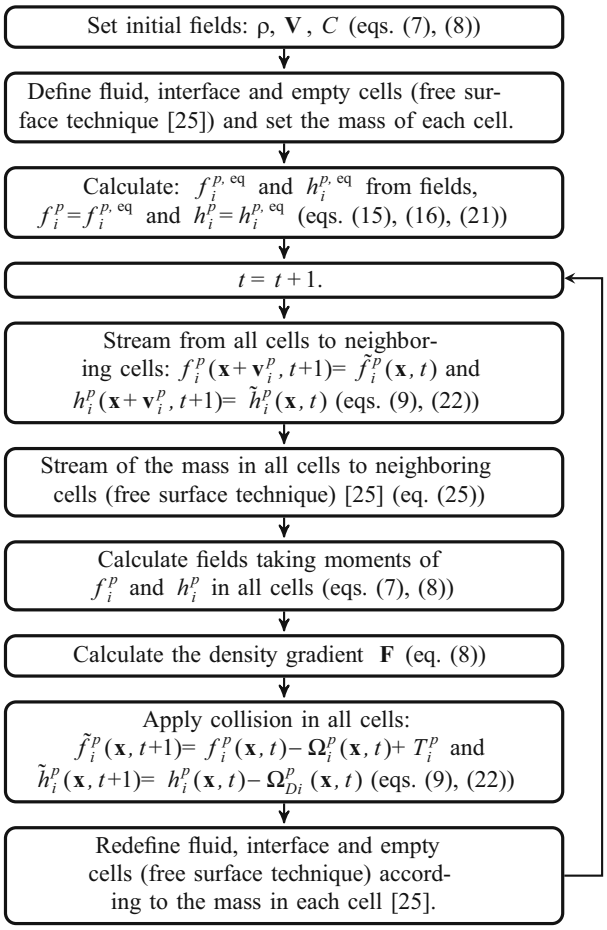

Fig. 2. Computational procedure of the LB simulation of flow of mixtures through anisotropic porous media including free surface and tension effects.

4 Algorithm implementation

To obtain a transparent, portable simulation code, we implemented it object-oriented. The general framework of a simulation is given in fig. 2. First, we set all initial field values like the density ρ, the velocity $\mathbf{V}$, the external force field $\mathbf{F}^{ext}$ (eqs. (7), (8)), and the solvent concentration C inside the mixture. To completely define the system, the porosity field, the permeability fields, and relaxation times are set. Also the initial saturation and boundary conditions like periodicity, pressures, flow rate, or impermeability are imposed. We can define three types of cells: fluid, interface and empty, depending on the problem. With these quantities set, we can start calculating the distribution functions f_i^p, h_i^p from the equilibrium distribution functions $f_i^{p,\mathrm{eq}}$ and $h_i^{p,\mathrm{eq}}$ (eqs. (15), (16), (21)). Now, the time step can be incremented and the system is ready to evolve (see fig. 2).

To follow the evolution of the system, we first solve the stream to all neighboring cells, stream their mass and calculate the macroscopic variables. Then the density gradient $\mathbf{F}$ is calculated. Finally, we have to update the type of cells and increment the time to prepare the system for the next time step. These steps are looped over all cells in the system. We stop the simulation, when a stable state is reached.

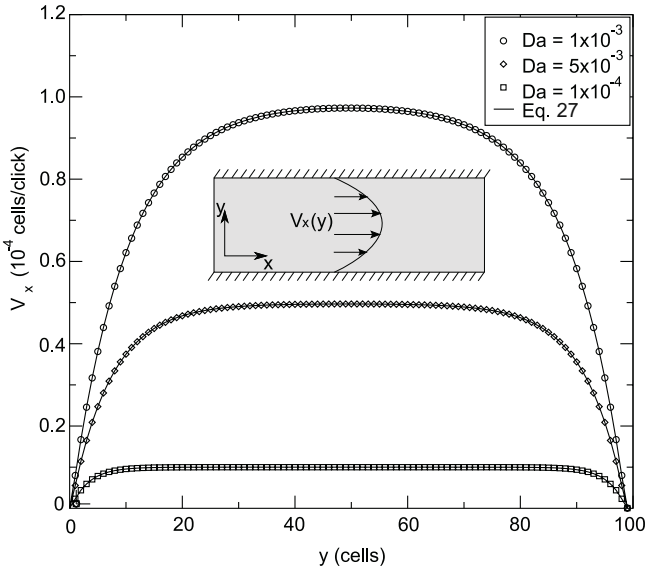

Fig. 3. Velocity profile for a generalized Poiseuille flow in a homogeneous, isotropic porous medium for various Darcy numbers. The generalized Poiseuille flow is obtained when the fluid moves through a channel between two walls driven by a constant body force through the porous medium (shaded zone).

5 Model validation and application examples

To validate our LB model implementation, we simulate systems with known analytical solutions that address each term from the generalized Navier-Stokes equations. In particular we simulate Poiseuille flow through isotropic and anisotropic porous media, droplet formation, and fluid surface smoothening. Finally, we show an application for the penetration of hardening mixtures into an anisotropic, heterogeneous porous medium, demonstrating the capability of the model to represent adhesive penetration in complex materials like wood.

5.1 Single fluid in homogeneous, isotropic porous media

To show the capability of the model to reproduce the Darcy law in a simple case, we simulate a generalized Poiseuille flow driven by a constant force in an isotropic, homogeneous medium between two infinite plates at distance L (see fig. 3). For this case, we need neither the surface tension tensor nor the free surface technique. Therefore just the force terms from the Darcy law, body force and the viscosity terms on the right-hand side of eq. (2) are active. We impose periodic boundary conditions on all velocity vectors and zero velocity at $y = 0, L$ of our 3D system. We only consider movements in the x-direction, so the velocity has the form $\mathbf{V} = (V_x, 0, 0)$ with boundary values of $V_x(x, 0) = V_x(x, L) = 0$. The analytical solution

of this problem is well known [1] by a Brinkman-extended Darcy equation, and has the form,

$$V_x(y) = \frac{GK}{\nu}\left(1 - \frac{\cosh[r(y - L/2)]}{\cosh[rL/2]}\right), \qquad (28)$$

where $r = \sqrt{\frac{\nu\epsilon}{K\nu_e}}$.

We set up a system of $3 \times 100 \times 1$ cells with porosity $\epsilon = 0.3$, relaxation time $\tau = 0.6$, density $\rho = 1.0$, and the body force $\mathbf{G} = (0.1, 0, 0)$. The permeability K is fixed by the Darcy number $Da = K/L^2$ to 10^{-3}, 5×10^{-3}, and 10^{-4}, respectively. We start with a flat profile and let the system evolve. When the velocity profile reaches a steady state, the simulation is stopped. Comparing the solution to eq. (28) we find excellent agreement with the theory (see fig. 3).

5.2 Anisotropic permeability validation

In order to validate the model for anisotropic porous media, we study Poiseuille flow like in sect. 5.1, but with a diagonal permeability tensor K, that was fixed to $\mathsf{K} = 10^{-3}\delta_{xx} + 10^{-5}\delta_{yy}$.

First, like before we let the fluid move inside the porous medium in x-direction with $V_x(y = 0, L) = 0$ at the bottom and top. In a second simulation the fluid moves in z-direction with $V_y(x = 0, L) = 0$ at the vertical boundaries. The velocity profiles can be calculated again by eq. (28). In the simulation we used an array of $70 \times 70 \times 1$ cells with the identical porosity, relaxation time, and density as previously. However, the body force is $\mathbf{G} = (0.1, 0, 0)$ for the first case and $\mathbf{G} = (0, 0.1, 0)$ for the second one. We use periodic boundary conditions as before, zero velocity at $y = 0, L$ for the first case, and $x = 0, L$ in the second case. We run the simulation until the system reaches a steady state and measure the respective velocity profiles (see fig. 4). The simulation results show that the model reproduces the Darcy flow in anisotropic porous media accurately.

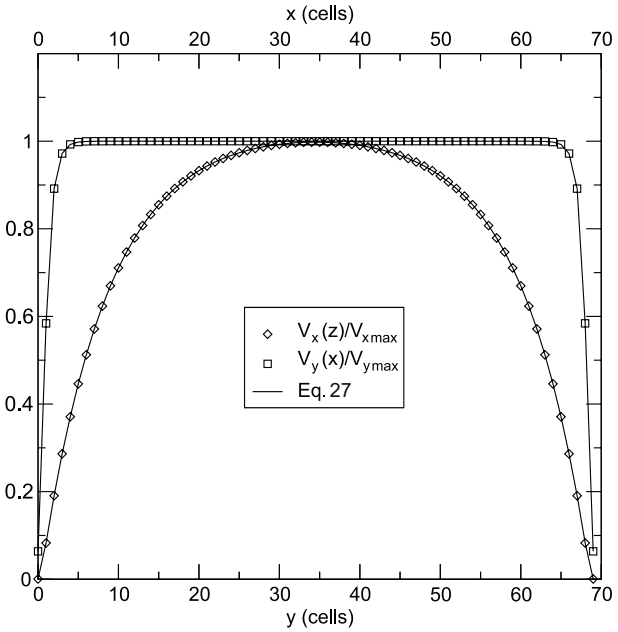

Fig. 4. Velocity profiles for an anisotropic porous medium with diagonal permeability tensor. Squares denote the velocity profile of the x component and diamonds represent the simulation with flow in y-direction ($v_{x,max} = 3 \cdot 10^{-3}$, $v_{y,max} = 3 \cdot 10^{-5}$).

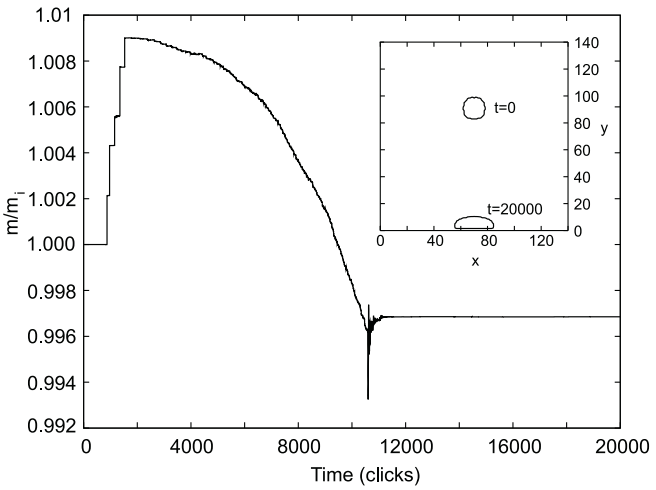

Fig. 5. Evolution of the total mass of a falling droplet that crashes against an impermeable and solid wall. Inset: snapshots of the droplet at initial time (top) and after 20000 time steps (bottom).

5.3 Free surface model test

As a condition for a valid implementation of the free surface technique, we have to assure that our model conserves mass. This can be tested by simulating a freely falling droplet followed by its collision against an impermeable, solid wall.

The system consists of a grid of $140 \times 140 \times 1$ cells. Initially a droplet with a radius of 8 cells is placed in the upper part of the system and an impermeable surface avoids its penetration through the bottom of the simulation zone at $y = 0$. The system parameters are the fluid density $\rho = 1.0$, the relaxation time $\tau = 0.7$, the external gravitational force $\mathbf{G} = 1 \cdot 10^{-6} \cdot (0, 1, 0)$. The impermeable wall is modelled by setting the macroscopic velocity in the respective cells to zero. The force terms from the Darcy law and surface tension are neglected here. Again, we impose periodic boundary conditions for all velocities at the left and right boundary.

In fig. 5 we plot the droplet mass as function of time. We can see that the mass is conserved with a small error of less than 1%. Note also that this error is within the range of common errors that go along with LB simulations. After approximately 10600 time steps we find an abrupt peak in the total mass due to the collision with the wall. Note that due to numerical reasons, for a short time mass is transferred to the boundary cells that represent the impermeable wall, but is returned in the next time steps,

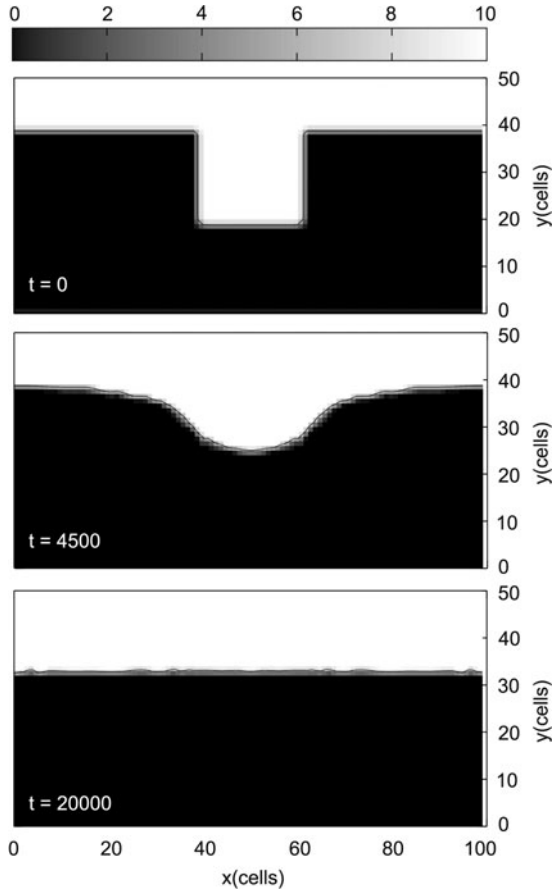

Fig. 6. Surface evolution due to surface tension from the initial shape (top panel) after 4500 time steps (center) and the steady state after 20000 time steps (bottom panel). Intensities represent the quantity of fluid in each cell, black cells are completely empty while white ones are completely filled.

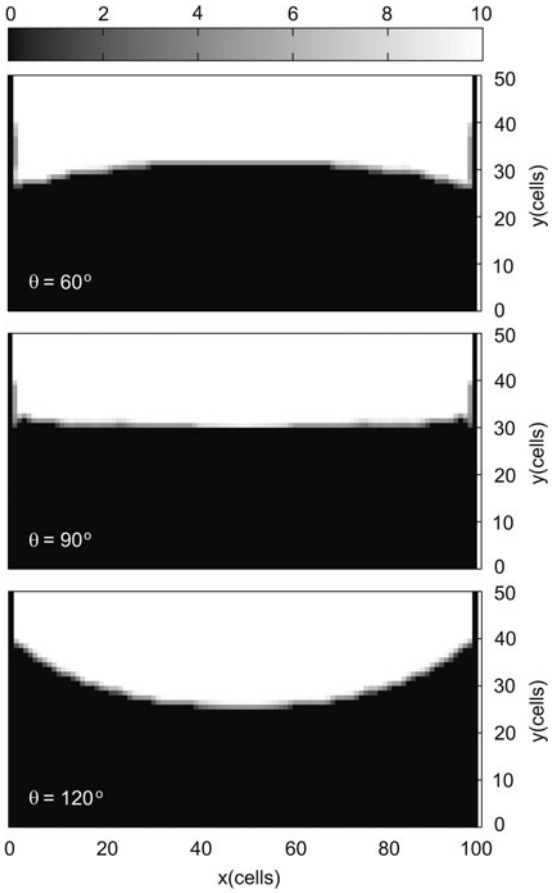

Fig. 7. Final fluid front shapes with solid walls at $x = 0$ and $x = 100$ with different wetting properties such that the contact angles are, respectively, from top to bottom panels: 60°, 90° and 120°. θ represents the analytical value. Intensities are identical to fig. 6.

so that the total mass recovers the value previous to the collision. The initial and configurations after 20000 time steps are shown in the inset of fig. 5. We clarify that the final configuration is not an equilibrium state due to the fact that there is no surface tension acting on the liquid to keep the shape of the droplet, therefore it will flatten in time.

5.4 Validation of the surface tension implementation

Mass conservation alone is not sufficient to describe free surfaces, rather surface tension needs to be considered. A correct implementation can be for example tested by simulating the shape evolution of an initially rectangular fluid front to a circular shape. We implemented a simulation using an array of $100 \times 50 \times 1$ cells, with an initially filled, square fluid zone of size 20×20 cells (see fig. 6). The density and relaxation time are identical to the droplet simulation, and a surface tension parameter of $A_g = 0.003$ was chosen (see eq. (16)). Periodic boundary conditions at left and right, and free boundary conditions on top and bottom are imposed. The force terms from the Darcy law, as well as external forces like gravity were switched off. The time evolution of the system is shown in fig. 6. We repeat the simulation with two solid walls at $x = 0, 100$ with different wettability properties such that the contact angles are 60°, 90° and 120°. All boundaries have non-slip conditions (all velocity components are zero) except the free boundary at the bottom of the simulation zone. After 30000 time steps the system reaches equilibrium and the final profile of the fluid is shown in fig. 7. We obtain errors around 5% between expected and obtained contact angles.

To finalize the validation of our surface tension approach, we simulate a sessile drop with different wettability of the solid substrate. We use the same parameter values as before and set the parameter A_s for expected contact angles θ_t of 60°, 90° and 120°. The gravity is decreased to $\mathbf{G} = 1 \cdot 10^{-7} \cdot (0, 1, 0)$ to facilitate the measurement of the contact angle during the simulation. The boundary conditions are periodic at the top, left and right, and non-slip at the bottom of the simulation zone. The initial configuration is a droplet of radius $R = 15$ cells located at $(50, 25, 0)$. After 50000 time steps the system reached the equilibrium state, shown in fig. 8. Between

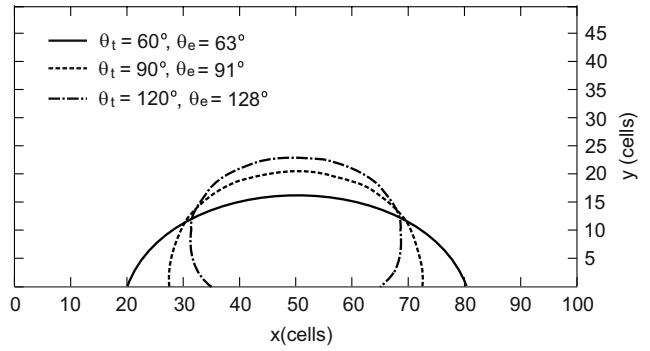

Fig. 8. Sessile drop simulation. The solid substrate is located at $z = 0$ with different wettability such that the contact angles are 60°, 90° and 120°. θ_t is the analytical value calculated by setting the parameter A_s, and θ_e represents the equilibrium contact angle obtained by the simulation.

the expected contact angles θ_t and the resulting ones θ_e we find differences of 6%.

Summarizing, we showed that the model can reproduce the theory of single fluids in the case of anisotropic porous media with surface tension effects and external forces. Note that the free surface technique should be only applied to liquids with low Reynold numbers.

5.5 Penetration of adhesives in wood

To demonstrate the applicability of our model, we describe the simulation of the penetration of adhesives into wood which is an anisotropic porous medium. The adhesives can be treated like two fluids: a polymer (solute) and a solvent, *e.g.* water. The polymer dynamics is governed by the advection-diffusion equation and the solvent by the generalized Navier-Stokes equations. To consider hardening effects in the adhesive, we have to consider a local change in time of the viscosity due to the change of concentration. An additional difficulty is the description of the anisotropic porous medium wood. We need to obtain the permeability tensor of wood and to implement a law for the dependency of the viscosity with the concentration and time.

Wood properties

In wood, the orthotropic permeability tensor and density are local properties, depending mainly on the year ring geometry, orientation, and position inside the year ring. Following refs. [34,35] an empirical expression of the wood density of the type

$$\rho(x) = \rho_0[1 + 2ax^b \exp(-cx)], \tag{29}$$

with the parameters a, b, c, the position x, and the minimum density ρ_0 can be made with parameters depending on the type of wood. For spruce we can take values of $\rho_0 = 310\,\mathrm{kg/m^3}$, $a = \frac{24}{\Delta}$, $b = 0.8$, and $c = \frac{9.6}{\Delta}$, where $\Delta = 2.9\,\mathrm{mm}$ is the year ring width [34]. To represent several parallel year rings, we use a periodic function of the form of eq. (29) with periodic Δ. Since wood consists of cell walls and lumen, we can estimate the porosity from the density by

$$\epsilon(x) = 1 - \frac{\rho(x)}{\rho_{max}}, \tag{30}$$

where ρ_{max} is the density of cell walls. Permeability and porosity are related in the scalar case by [1]

$$K = \frac{\epsilon^3}{n(1-\epsilon)^2} D_p^2, \tag{31}$$

with the characteristic pore size D_p and a constant n that parametrizes the microscopic geometry of the material taken as $n = 150$ in our case. In wood, the pore size D_p must also depend on the wood density, and we propose as a first approximation the relation

$$D_p(x) = C_2 \left(1 - \frac{\rho(x)}{\rho_{max}}\right)^{\frac{1}{3}}, \tag{32}$$

with a constant C_2, that can consider the shape of the microscopic pores [36]. Inserting eqs. (30) and (32) in eq. (31) we obtain the macroscopic permeability of a sample as a function of the year ring coordinate x. C_2 can now be obtained by integrating eq. (31) over one year ring and comparing it to literature values for the macroscopic permeability [37,38] of spruce in radial, longitudinal, and tangential direction. We finally calculate the required local permeability tensor in cylindrical coordinates (r, z, θ), as

$$\mathsf{K} = \left(\frac{\rho_{max}}{\rho(x)}\right)^2 \epsilon(x)^{\frac{11}{3}} \begin{pmatrix} 8.2 & 0 & 0 \\ 0 & 51470 & 0 \\ 0 & 0 & 0.82 \end{pmatrix} \times 10^{-10}\,\mathrm{mm}^2. \tag{33}$$

Hardening process and viscosity model

To determine the viscosity evolution during the hardening process, we have to take into account two main factors: the chemical reactions that take place between the adhesive molecules and the solute concentration. The first factor causes a viscosity increment with time, while due to the second one, viscosity changes with local solvent concentrations. In order to describe these mechanisms, we choose a viscosity model given by

$$\nu(C,t) = \nu_g[1 + a\exp(\alpha t)]\exp(\beta[1 - C]), \tag{34}$$

where ν_g, a, α, and β are parameters that can be obtained from experimental hardening curves of adhesives with diverse solvent concentration.

Simulation of adhesive penetration into wood

Embedding the permeability tensor field and the hardening function, our model is ready to simulate the penetration of adhesives into the porous wood mesostructure.

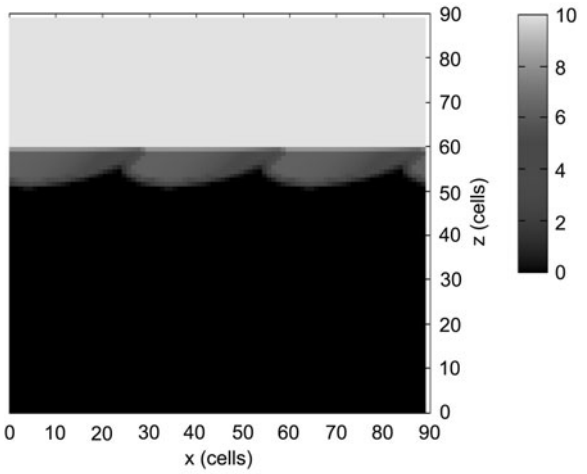

Fig. 9. Fluid profile during the penetration into the wood structure. Intensities are identical to fig. 6. The wood sample is located in the region $y < 60$ with a year ring inclination of 45°.

We use an array of $90 \times 90 \times 1$ cells and locate the wood sample in the zone $y < 60$. The year rings are inclined by 45° to the horizontal plane. We take the fluid density $\rho = 1.0$, the parameters for the porosity, according to eq. (29) with $a = 0.62$, $b = 0.2$, and $c = -0.2$, corresponding to spruce wood [34], and a year ring distance Δ of 30 cells. The viscosity model uses the parameters $\nu_g = 0.15$, $a = 2.05 \times 10^{-9}$, and $\beta = 10^{-3}$, obtained from viscosimetric measurements with urea formaldehyde adhesive [39]. Additionally, we applied a constant external pressure of $P_{ext} = 0.0441$ that is equivalent to $0.9\,\mathrm{mN/mm^2}$ in IS units. In the simulation we use periodic boundary conditions at the left and right edge, and free boundary conditions at the bottom and top of the simulation zone.

The simulation was stopped when the adhesive could not penetrate further due to hardening. Figure 9 shows the penetration of the fluid into the wood sample. We can see that the model can simulate complex materials like wood. In some zones the adhesive penetrates with more speed due to the higher local porosity and the direction of the movement is correlated with the principal axis of the permeability tensor.

6 Discussion and conclusions

We introduced a new lattice Boltzmann model to simulate the dynamics of the flow of mixtures in anisotropic, heterogeneous porous media. Our 3D model can be applied to many problems in material science and engineering. It includes a free surface technique to simulate the invaded fluid profile inside the material structure and a surface tension term to control the interface dynamics, the cohesion inside the fluid, and the wettability properties of solid substrates.

The accuracy of the model was tested for a set of simple cases, like generalized Poiseuille flow in isotropic and anisotropic porous media, droplet formation, surface smoothing for various boundary conditions and sessile drop formation. We found excellent agreement with the Darcy law for Poiseuille flow. The free surface technique is validated in the simulation of a freely falling droplet and its collision against an impermeable surface showed negligible errors. The surface tension effects were tested by simulating the smoothing of the fluid front, first with periodic boundary conditions and then with vertical solid walls with different wettability properties derived from different contact angles. Also we implemented simulations of sessile droplets for different contact angles and found small desviations of 6%. To demonstrate the applicability of the model to real cases, we implemented a simulation of the penetration of adhesives into a sample of spruce wood. We showed that the model can reproduce the dynamics of hardening fluids in complex materials even when the media are anisotropic and heterogeneous.

The actual model has all the advantages known for the lattice Boltzmann method like the minimal use of computational resources, fast algorithms that allow for real-time simulations, and the ability for efficient parallelization. Additionally, extensions of the model are rather straightforward. We hope that the proposed simulation approach will be useful in order to model complex geometries in heterogeneous and anisotropic porous media even for complicated fluids like mixtures of two components.

The authors are grateful for the financial support of the Swiss National Science Foundation (SNF) under grant no. 116052.

References

1. K. Vafai, *Handbook of POROUS MEDIA*, second edition (Taylor and Francis Group, LLC, 2005).
2. A. Morais, H. Seybold, H. Herrmann, J.S. Andrade Jr., Phys. Rev. Lett. **103**, 194502 (2009).
3. C.L. Tien, K. Vafai, Adv. Appl. Mech. **27**, 225 (1990).
4. C.T. Hsu, P. Cheng, Int. J. Heat Mass Transf. **33**, 1587 (1990).
5. P. Nithiarasu, K.N. Seetharamu, T. Sundararajan, Int. J. Heat Mass Transf. **40**, 3955 (1997).
6. J. Bear, *Dynamics of Fluids in Porous Media*, first edition (Dover Publication, 1972).
7. F. Kamke, J. Lee, Wood Fiber Sci. **39**, 205 (2007).
8. G.R. McNamara, G. Zanetti, Phys. Rev. Lett. **61**, 2332 (1988).
9. F. Higuera, S. Succi, R. Benzi, Europhys. Lett. **9**, 345 (1989).
10. E.G. Flekkoy, Phys. Rev. E **54**, 5041 (1993).
11. B. Chopard, M. Droz, *Cellular Automata Modelling of Physical Systems*, 12th edition (Cambridge University Press, 1998).
12. B. Chopard, P. Luthi, J. Wagen, IEE Proc. Microwave Antennas Propag. **144**, 251 (1997).
13. S. Succi, R. Benzi, M. Vergassola, Phys. Rev. A **4**, 4521 (1991).
14. S. Chen, H. Chen, D. Martinez, W. Matthaeus, Phys. Rev. Lett. **67**, 3776 (1991).
15. M. Mendoza, J.D. Munoz, Phys. Rev. E **77**, 026713 (2008).
16. S. Succi, R. Benzi, Physica D **69**, 327 (1993).

17. T. Reis, T.N. Phillips, J. Phys. A: Math. Theor. **40**, 4033 (2007).
18. M. Latva-Kokko, D.H. Rothman, Phys. Rev. E **72**, 046701 (2005).
19. D. Grunau, S. Chen, K. Eggert, Phys. Fluids A **10**, 2557 (1993).
20. J. Chin, E.S. Boek, P.V. Coveney, Philos. Trans. R. Soc. London, Ser. A **360**, 547 (2002).
21. X. Shan, H. Chen, Phys. Rev. E **47**, 1815 (1992).
22. A.K. Gunstensen, D.H. Rothman, Phys. Rev. A **43**, 4320 (1991).
23. J. Tolke, M. Krafczyk, M. Schulz, E. Rank, Philos. Trans. R. Soc. London, Ser. A **360**, 535 (2002).
24. Z. Guo, T.S. Zhao, Phys. Rev. E **66**, 036304 (2002).
25. C. Korner, R.F. Singer, *Metal Foams and Porous Metal Structures* (MIT Publishing, 1999) pp. 91–96.
26. D.J. Korteweg, Arch. Néerl. Sci. Exactes Nat. Ser. II **6**, 1 (1901).
27. T. Reis, T.N. Phillips, J. Phys. A: Math. Theor. **40**, 4033 (2007).
28. D.M. Anderson, G.B. McFadden, W.A, Annu. Rev. Fluid Mech. **30**, 139 (1998).
29. P. Bathnagar, E. Gross, M. Krook, Phys. Rev. **94**, 511 (1954).
30. Z. Guo, C. Zheng, B. Shi, Phys. Rev. E **65**, 046308 (2002).
31. S. Succi, *The Lattice Boltzmann Equation for Fluid Dynamics and Beyond*, first edition (Oxford University Press, 2001).
32. U. Frisch, D. d'Humires, B. Hasslacher, P. Lallemand, Y. Pomeau, J.P. Rivet, Complex Syst. **1**, 649 (1987).
33. A. Hiorth, U.H.A. Lad, S. Evje, S.M. Skjaeveland, Int. J. Numer. Methods Fluids **59**, 405 (2009).
34. F. Wittel, G. Dill-Langer, B. Kroeplin, Comput. Mater. Sci. **32**, 594 (2004).
35. O. Bouriaud, N. Bréda, G.L. Moguédec, G. Nepveu, Trees **18**, 264 (2004).
36. L. Gibson, M. Ashby, *Cellular Solids: Structure and Properties* (Cambridge University Press, 1999).
37. N. Mouchot, A. Zoulalian, Holzforschung **56**, 318 (2002).
38. P. Perre, A. Karimi, Maderas Cienc. Tecnol. **4**, 50 (2002).
39. F.W.H.J. Herrmann, P. Niemz, Technical report, Institute for Building Materials (2009).